

# Molecular dynamics simulation of delamination of a stiff, body-centered-cubic crystalline film from a compliant Si substrate

L. M. Hale,<sup>1,a)</sup> X. W. Zhou,<sup>2</sup> J. A. Zimmerman,<sup>2</sup> N. R. Moody,<sup>3</sup> R. Ballarini,<sup>4</sup> and W. W. Gerberich<sup>1</sup>

<sup>1</sup>*Department of Materials Science, University of Minnesota, Minneapolis, Minnesota 55455, USA*

<sup>2</sup>*Department of Mechanics of Materials, Sandia National Laboratories, Livermore, California 94550, USA*

<sup>3</sup>*Department of Analytical Materials Science, Sandia National Laboratories, California 94550, USA*

<sup>4</sup>*Department of Civil Engineering, University of Minnesota, Minneapolis, Minnesota 55455, USA*

(Received 24 June 2009; accepted 6 September 2009; published online 16 October 2009)

Compliant substrate technology offers an effective approach to grow high-quality multilayered films, of importance to microelectronics and microelectromechanical systems devices. By using a thin, soft substrate to relieve the mismatch strain of an epitaxial film, the critical thickness of misfit dislocation formation in the overlayer is effectively increased. Experiments have indicated that stiff films deposited onto Si substrates can delaminate at the interface. However, the atomic mechanisms of the deformation and the fracture of the films have not been well studied. Here, we have applied molecular dynamics simulations to study the delamination of a stiff body-centered-cubic crystalline film from a compliant Si substrate due to tensile loading. The observed mechanical behavior is shown to be relatively independent of small changes in temperature, loading rate, and system size. Fracture occurs at the interface between the two materials resulting in nearly atomically clean surfaces. Dislocations are seen to nucleate in the body-centered-cubic film prior to delamination. At higher strains, a phase change to a face centered cubic is observed within the body-centered-cubic film, facilitating extensive dislocation growth and interaction. The various defects that form prior to fracture are discussed and related to the mechanical properties of the system. © 2009 American Institute of Physics. [doi:10.1063/1.3238521]

## I. INTRODUCTION

As electronic devices shrink in scale, their properties become increasingly sensitive to the structural defects. Compliant substrate technology has become a potent approach to control defects in complicated multilayer structures composed of lattice-mismatched materials. By choosing a thin, soft substrate for an overlayer film, it is hoped that the substrate will elastically respond to the mismatch strain, relieving some of the strain present within the epitaxial overlayer. This strain relief can increase the critical thickness for misfit dislocation formation in the overlayer, thereby significantly reducing the dislocation density.

As Si is the primary material used in microelectronics and microelectromechanical systems devices, its use as a substrate material has been extensive. Although Si is brittle, it has relatively low elastic moduli compared to some metals (e.g., W). As a result, Si is of considerable interest as a compliant substrate for these stiff metals. Previous studies have indicated that stiff films on compliant substrates often fail through buckling and cracking.<sup>1</sup> Here, molecular dynamics (MD) simulations are performed to examine the effects of tensile loading of a model body-centered-cubic (bcc) film on a Si in order to help understand the fundamental origins of these failure mechanisms. In particular, the mechanical behaviors of the film and substrate prior to and during delamination are presented.

In this paper, we first examine the effects of varying the simulation conditions on the resulting observed behavior of the yielding and fracturing of the films. Next, the fracture behavior is characterized. Finally, we explore the details of the yielding behavior, where, in addition to dislocations, a bcc-to-fcc transition is discovered to occur at high strains. Stress induced transitions of this type have recently been simulated for Fe at crack tips<sup>2</sup> and have experimentally been observed in severely deformed nanocrystalline steel<sup>3</sup> but have not been shown for other bcc materials such as Mo and W. Explanations for how this behavior occurs in the current simulations and facilitates dislocation motion are provided.

## II. METHOD

### A. Interatomic potentials

The interactions between the Si atoms were modeled by a Tersoff potential using the parameters given by Tersoff for good elastic constant predictions.<sup>4,5</sup> The interactions between the model bcc metal (M) atoms were modeled using the analytical embedded atom method approach<sup>6–8</sup> with the parameters listed in Table I. A Morse potential,  $\phi(r)=0.8\{\exp[-4(r-3)]-2\exp[-2(r-3)]\}$ , for  $r$  in angstrom and  $\phi$  in eV, was used for the cross interaction between M and Si atoms.

For our applications, the material properties such as the lattice constants, the cohesive energies, the elastic constants, the surface energies, and the increases in energy during phase transformations are all important. The lattice constants affect lattice mismatch. The cohesive and surface energies are key parameters regarding fracture strength. The elastic

<sup>a)</sup> Author to whom correspondence should be addressed. Tel.: +925-294-6063. FAX: +925-294-3747. Electronic addresses: lhale@cems.umn.edu and lmhale@sandia.gov.

TABLE I. Embedded atom method potential parameters used for metal M.

$r_e$ (Å)	$f_e$	$\rho_e=\rho_s$	$\alpha$	$\beta$	A (eV)	B (eV)
2.740 840	3.487 340	37.234 847	8.900 114	4.746 728	0.882 435	1.394 592
$\kappa$	$\lambda$	$F_{n0}$ (eV)	$F_{n1}$ (eV)	$F_{n2}$ (eV)	$F_{n3}$ (eV)	$F_0$ (eV)
0.139209	0.278417	-4.946 281	-0.148 818	0.365 057	-4.432 406	-4.96
$F_1$ (eV)	$F_2$ (eV)	$F_3$ (eV)	$\eta$	$F_e$ (eV)	$\mu$	$\nu$
0	0.661 935	0.348 147	0.582 714	-4.961 306	0.85	1.15

constants determine the relative compliance of the materials and the dislocation energy (which, in turn, affects the elastic and plastic behaviors). Finally, the increases in energy due to the phase transformations determine both the deformation path (e.g., the phase transformation deformation mechanism of shape-memory alloys) and the stability of the bcc phase. The predicted values of these properties for the Si potential used have been previously published.<sup>4,5,9</sup> The values for the M potential were calculated here. All of the relevant properties predicted by both potentials are listed in Tables II and III, along with experimentally determined values for Si.<sup>9,10</sup> It should be noted that although M is being considered as a model element in the work presented here, its lattice constant, cohesive energy, elastic constants, and surface energies closely match with the experimental values of W.<sup>11-15</sup> In addition, the model for M correctly predicts an increase in energy due to a bcc to face-centered-cubic (fcc) phase change. The cross interaction was tuned to correctly predict the pressure profiles experimentally observed in W on Si films.<sup>16</sup>

## B. MD model

Direct MD simulations of the deposition of W on a {010} Si surface<sup>16</sup> indicated that W grows into a {010} textured bcc crystal with its  $\langle 100 \rangle$  directions parallel to the  $\langle 101 \rangle$  directions of the {010} Si surface. As the lattice constant and other properties of our modeled M element match the properties of W, this type of interface was selected for study in this work. Our system assumes that the interface between the two materials lies on the global  $x$ - $z$  plane, and the tensile loading is applied in the  $y$ -direction corresponding to the [010] direction in both materials. Accordingly, the  $x$ -,  $y$ -, and  $z$ -axes of the global system are aligned with the [101], [010], and  $[\bar{1}01]$  directions of Si and with the [100], [010], and [001] directions of M. The system size in the  $x$ - and  $z$ -directions was chosen to be about 126.75 Å. This closely fits both 33 repeat units of Si {101} planes and 40 repeat units of M {100} planes, with a low mismatch strain in the M of about -0.000 69. Periodic boundary conditions were imposed in the  $x$ - and  $z$ -directions. The film was given a finite thickness

in the  $y$ -direction with the atoms in the outermost 15 Å on both free surfaces being held at perfect bulk lattice positions.

A reasonable interfacial structure was created by first positioning the M crystal above (positive  $y$ -direction) the Si crystal with a gap between the two materials slightly larger than the expected atomic spacing. Next, a molecular statics simulation was carried out to minimize the system energy and relax the interfacial structure. Finally, the interface was further allowed to relax through the use of a MD simulation at the simulated temperature with no applied loads. In this work, the  $x$ - and  $z$ -dimensions were held constant, and a Nose/Hoover thermostat<sup>17</sup> was used to control the temperature. An example of the simulated M/Si system containing a relaxed interface is shown in Fig. 1. We found that following the relaxation process, rippled structures developed at the interface, similar to what was previously observed in Ni/Si and Al/Si systems.<sup>18</sup> The rippling occurred due to M and Si atoms at the interface moving to fill the gaps produced by the mismatch between the two lattices.

To apply a tensile strain to the system, constant temperature MD simulations were performed where the bottom 15 Å of Si atoms was fixed and the top 15 Å of M atoms was constrained to move at a constant rate. A gauge length was specified within the specimen prior to the test, and all atoms within that section were identified. The change in length during the test was determined by finding the maximum and minimum  $y$ -coordinate for the atoms that were contained within the initial gauge length. The applied stress was calculated as the average virial stress<sup>19</sup> over all of the gauged atoms. All simulations were performed using the LAMMPS software.<sup>20</sup>

## III. RESULTS

### A. Stress versus strain relationships

The simulations were carried out at accelerated strain rates in the range of  $10^8$ – $10^9$  s<sup>-1</sup>. To explore the effects of these accelerated strain rates and the small sample dimensions of the simulation systems, stress versus strain curves were calculated for simulation runs with varying strain rates

TABLE II. Lattice constant  $a$  (Å), cohesive energy  $E_c$  (eV/atom), elastic constants  $C_{11}$  (GPa),  $C_{12}$  (GPa), and  $C_{44}$  (GPa), and energy increase  $\Delta E_{\text{bcc} \rightarrow \text{fcc}}$  (eV/atom) during the bcc  $\rightarrow$  fcc phase transformation. Calculated values of Si and experimental values (in parentheses) are from Ref. 9.

Element	$a$	$E_c$	$C_{11}$	$C_{12}$	$C_{44}$	$\Delta E_{\text{bcc} \rightarrow \text{fcc}}$
M	3.165	-8.76	522.5	204.2	160.8	0.16
Si	5.43 (5.43)	-4.63 (-4.63)	143 (167)	75 (65)	69 (81)	...

TABLE III. Surface energies  $\gamma$  (J m<sup>-2</sup>) for various surfaces. Calculated values of Si are from Ref. 9, and experimental values (in parentheses) are from Ref. 10.

Element	{010}	{011}	{111}
M	2.98	2.56	3.32
Si	2.31 (2.13)	1.57 (1.51)	1.29 (1.23)

and sample thicknesses at a fixed temperature of 300 K. The results are shown in Fig. 2. Figure 2(a) compares the behavior of two systems with different sample thicknesses both subject to the same strain rate of  $2.88 \times 10^9$  s<sup>-1</sup>, while Fig. 2(b) shows the effect of two different strain rates at the same sample thickness ( $\sim 87$  Å M and  $\sim 107$  Å Si). The oscillation during elastic loading seen in Fig. 2 is known to result from a shockwave created during accelerated tensile loading.<sup>18</sup> The effect of the shockwave is effectively eliminated by using the relatively low strain rate of  $2.97 \times 10^8$  s<sup>-1</sup>, as seen in Fig. 2(b). It can be seen that the results, especially the elastic deformation and initial yielding, are not sensitive to the system dimension and strain rate within the explored ranges.

The stress versus strain curves were also measured at two additional low temperatures of 20 and 50 K with a fixed strain rate of  $2.88 \times 10^9$  s<sup>-1</sup> and a fixed sample thickness of  $\sim 87$  Å M and  $\sim 107$  Å Si. It was found that this change in temperature also did not affect the initial yielding.

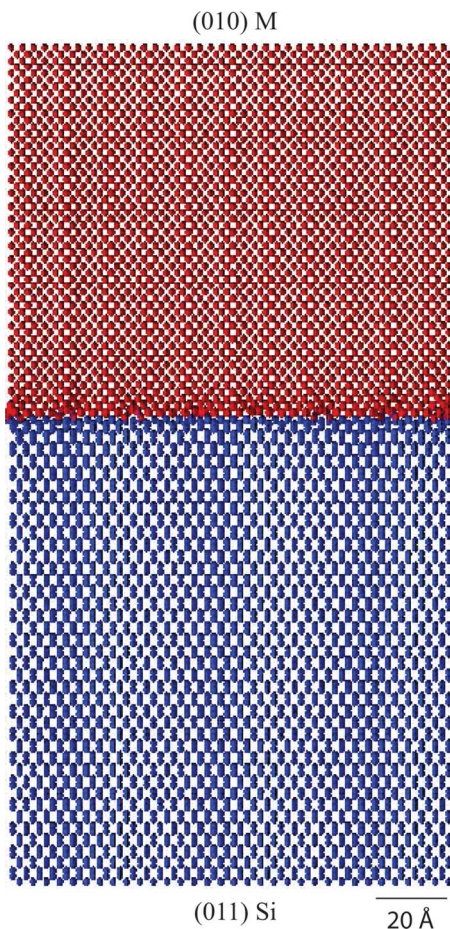


FIG. 1. (Color online) Front view of the simulated system.

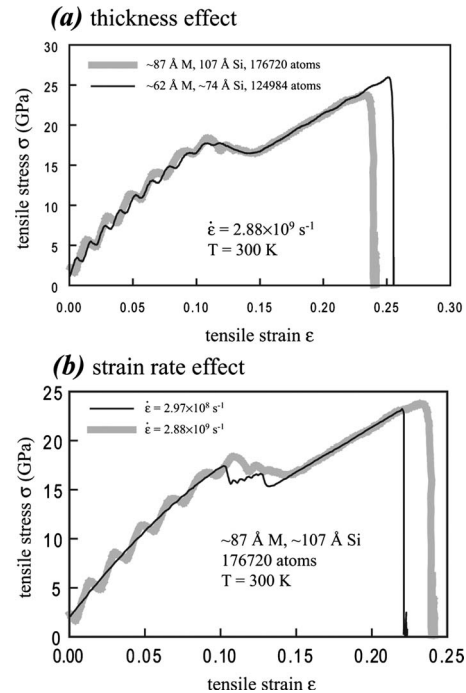


FIG. 2. (a) Thickness and (b) strain rate effects on stress vs strain curves.

Figure 2 shows that upon loading, the specimen initially deformed elastically before yielding at a strain of approximately 0.1. Strain hardening can be seen following the yield up until the fracture occurred at a strain of  $\sim 0.25$ . To isolate the deformation behavior occurring in each material, two additional gauge lengths were specified: one containing only Si atoms and the other containing only M atoms. These smaller gauge lengths allowed for stress versus strain plots to be developed for each component material in the composite system. Two examples of the stress versus strain plots, measured respectively for M and Si, are shown in Figs. 3(a) and 3(b), respectively. As indicated in Fig. 3(a), M shows three expected stages of behavior: elastic deformation, extensive yielding, and strain hardening. In contrast, Fig. 3(b) shows that Si behaves elastically over the entire strain range explored, although the elastic behavior deviates from linearity at large strains. The plastic yielding within M will be further explored through an analysis of dislocation motion.

Because no shockwave was observed at the slower strain rates and temperature and sample thickness had little effect on the overall behavior over the range explored, the remaining analysis focused solely on one tested case: sample thicknesses of  $\sim 87$  Å (M) and  $\sim 107$  Å (Si), strain rate of  $2.97 \times 10^8$  s<sup>-1</sup>, and temperature of 300 K.

## B. Fracture observation

The evolution of atomic scale configurations around the time of fracture has been examined, and one example is shown in Fig. 4. An analysis of the images showed that cracks initiated at one point along the interface and then proceeded to expand outward along the interface. This is consistent with the previous observations for Al/Si interfaces<sup>18</sup> that cracks initiated at the highly strained sites of the rippled interface. As the crack propagated along the in-

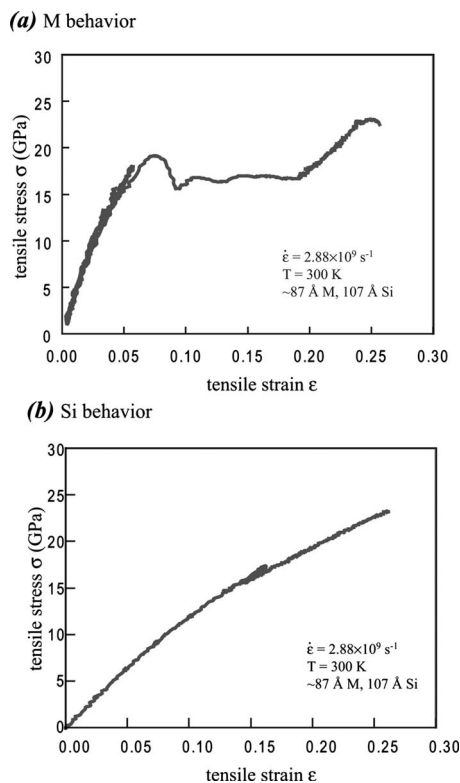


FIG. 3. Isolated (a) M and (b) Si behavior.

interface [Figs. 4(b) and 4(c)], Si developed a wavy appearance as the regions that had separated from the M attempted to relax to their unstrained positions while other regions remained attached. This is best seen in the diagonal view of the system [Fig. 4(c)]. It further confirms that Si is relatively more compliant than M. The complete fracture [Fig. 4(d)] resulted in the formation of atomically clean M and Si surfaces. However, while the fractured Si surface remained atomically flat, the M surface appeared to contain many steps characteristic of dislocation motion.

### C. Slip mechanisms at a small strain (<0.12)

To more clearly show the defects that formed within the M during loading, parameters that distinguish defects from a

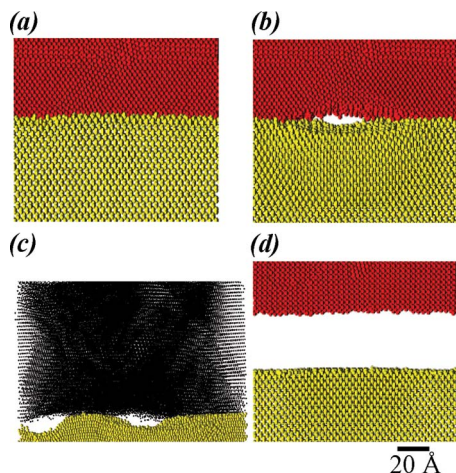


FIG. 4. (Color online) Interfacial fracture process. (a) Prior to crack formation, (b) during crack propagation, (c) another view of the crack propagation, and (d) after fracture.

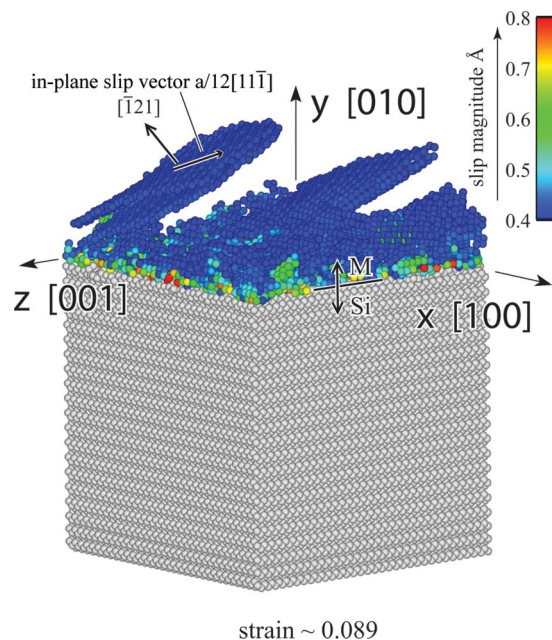


FIG. 5. (Color online) Slip configuration of a system at a relatively small strain of 0.089. For M, only atoms with slip magnitudes between 0.40 and 0.80 Å are shown.

perfect lattice are needed. Here, we use the slip vector parameter developed previously.<sup>21</sup> The slip vector is defined as  $\vec{S}_i = -1/N_s \sum_{j \neq i} (\vec{R}_{i,j} - \vec{R}_{i,j}^0)$ , where  $N$  is the total number of nearest neighbors to atom  $i$ ,  $N_s$  is the number of neighbors that are on an adjacent slip plane to atom  $i$  (e.g.,  $N_s = 3$  if slip occurs on a  $\{111\}$  fcc lattice),  $\vec{R}_{i,j}^0$  is the vector from atoms  $i$  to its neighbor  $j$  at an initial reference configuration, and  $\vec{R}_{i,j}$  is the corresponding vector at the current configuration. By finding the relative displacement of the nearest neighbor atoms  $j$  with respect to a given atom  $i$ , it can be determined if a plane neighboring atom  $i$  has slipped and in what direction. Dividing by  $-N_s$  scales the vector's magnitude so that it will be equal to the Burgers vector of the dislocation that caused the slip.

The deformation mechanisms present during the simulations have been explored by mapping the magnitude of the slip vector to the atom configurations. This analysis revealed no defects within the Si and therefore confirmed that Si remained elastic prior to the fracture. In sharp contrast, significant defects were seen in M. Here, we first demonstrate the defects formed in M at relatively small strains. One typical example is shown in Fig. 5 for a strain of 0.089. To improve the quality of the demonstration, the image was made after an energy minimization simulation was applied to relax the atom positions while under the applied strain. In Fig. 5, all Si atoms are colored white, whereas M atoms are colored according to the magnitude of the slip vector with the color scaled so that atoms with slipped distances outside of the 0.4–0.8 Å range are invisible. Figure 5 clearly reveals slipped planes that formed during the early stage of loading. The slip occurred due to the emission of dislocations into M from the interface primarily at the rippled sites where the mismatch stress was the highest. The onset of dislocation emission corresponded well with the yielding of the system.

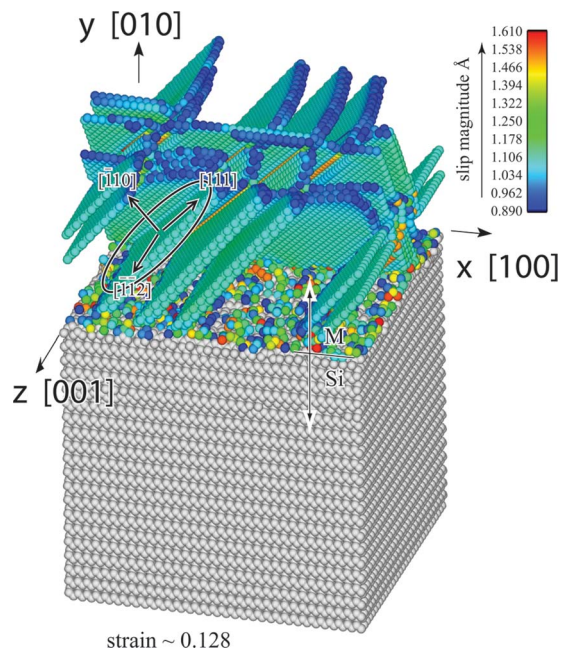


FIG. 6. (Color online) Slip configuration of a system at a relatively large strain of 0.128. For M, only atoms with slip magnitudes between 0.89 and 1.61 Å are shown.

Figure 5 shows that the magnitude of the slip vector is  $\sim 0.45$  Å. If the crystallographic orientations are referenced with respect to bcc M, then it can be seen that slip occurred on a  $(\bar{1}21)$  plane and that the in-plane slip vector is  $\frac{1}{12}[\bar{1}1\bar{1}]$ . This type of slip has a Schmid factor of 0.471. It is therefore a favorable system for slip and is expected in bcc systems.<sup>22,23</sup> In addition, it can be seen that the slip planes are wavy and ill defined, which is also consistent with the bcc lattice where slip planes can be a local combination of  $\{110\}$  and  $\{112\}$  planes.<sup>24</sup>

#### D. Slip mechanisms at a large strain ( $>0.12$ )

A similar analysis of the slip vector has also been used to study the defects in M at large strains. As an example, Fig. 6 shows the slip configuration of the system at a strain of  $\sim 0.128$ , where atoms with a slipped distance outside of the 0.89–1.61 Å range are invisible. Figure 6 clearly reveals extensive slipped planes that formed at the late stage of the tensile loading. Examinations indicated that the slip planes are of the  $\{110\}$  type. Nonparallel  $\{110\}$  planes interact to form a network of rectangular pipes along the  $\{111\}$  direction. It can be seen that the yielding observed in Fig. 2 corresponds well with the extensive slip seen in Fig. 6.

Analyses indicated that during the loading, the leading partial dislocations are nucleated at the interface and then quickly swept through the crystal. If the strain is not significant enough to nucleate voids, the trailing partial dislocations can be pinned at the interface. This resulted in the formation of the observed structure of the slipped planes. To further examine the slipped nature and the Burgers vector of the partial dislocations, four consecutive  $(\bar{1}10)$  planes in a circular region indicated in Fig. 6 are shown in Fig. 7, with the  $[\bar{1}10]$  direction coming out of the image and the circles rep-

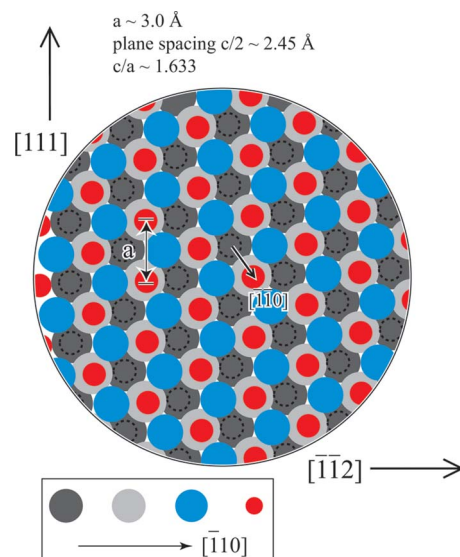


FIG. 7. (Color online) A projection of four consecutive  $(\bar{1}10)$  planes in the circular region shown in Fig. 6. The top two planes (the full large circles and the small circles) have slip magnitudes between 0.89 and 1.61. The dashed circles indicate the “correct” sites if the red atoms did not slip.

resenting the atoms ordered as shown in the legend. As a reference for comparing the two images, note that the lower two planes of atoms shown in Fig. 7 are invisible in Fig. 6 as they have relatively small slip distances, and only the fully seen large and small atoms shown in Fig. 7 are also visible in Fig. 6.

Figure 7 reveals several interesting phenomena: the symmetry of the planes is hexagonal; the ratio of the double plane spacing to in-plane atom spacing is about 1.633; and the three consecutive planes (large circles) are stacked in an “ABC...” sequence. Note that the large slip distance calculated for the top two planes of atoms is due to the relative shift between these planes and that no significant shift has occurred between other atoms. The stacking of the large circle atoms is therefore representative of the majority of regions where the shift is not significant. The observations made above indicate that these regions have transformed to a fcc structure.

The dashed circles in Fig. 7 mark the positions where the small atoms should be for a fcc structure had slip not occurred between the top two planes of atoms. By comparing the position of the small atoms with dashed circles, we find that the small atoms have slipped in the  $[\bar{1}\bar{1}0]$  direction in reference to the original bcc structure. Note that the Schmid factor for the critical resolved shear stress upon the  $(\bar{1}10)$  plane is the highest in the observed  $[110]$  slip direction with a value of 0.5. The Schmid factor is reduced to 0.408 in the bcc close-packed direction  $[111]$ . By accounting for the phase change and converting to the crystallographic orientations of the fcc structure, the slip plane is seen to essentially be  $\{111\}$ , and the Burgers vector of the slip is seen to correspond to  $\frac{1}{6}\langle 11\bar{2} \rangle$  partial dislocations. These observations are related to the Bain relation shown in Fig. 8, where we can see that the bcc lattice can be represented as a face-centered-tetragonal lattice that can transform to a fcc lattice during a

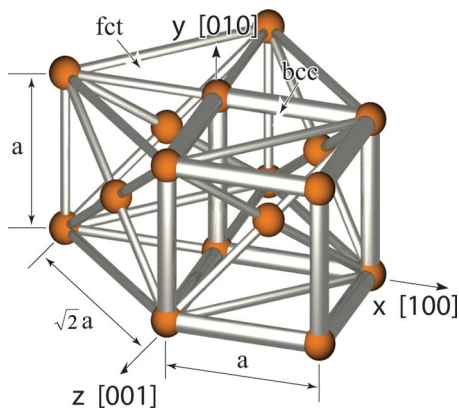


FIG. 8. (Color online) bcc-to-fcc transformation (Bain) mechanism.

uniaxial extension in the  $y$ -direction. In particular, we can see that the bcc  $(\bar{1}10)$  plane is essentially a (transformed) fcc  $\{111\}$  plane, and the bcc  $[\bar{1}\bar{1}0]$  direction is essentially a fcc  $\langle 11\bar{2} \rangle$  direction. The observed behavior therefore agrees with the  $\frac{1}{6}\langle 11\bar{2} \rangle \{111\}$  slip systems being commonly encountered in the fcc crystals.

The finding obtained in the present work suggests an interesting deformation mechanism that may not be known previously. When a bcc material is subject to a high strain, the lattice may be elastically distorted toward a fcc lattice. The  $\frac{1}{6}\langle 11\bar{2} \rangle \{111\}$  types of fcc slip systems can then be activated and contribute to the plastic deformation. When the stress is removed, the lattice can elastically recover to bcc. However, dislocations created during the slip are retained. These dislocations in the bcc lattice have apparent slip planes of  $\{110\}$  and an apparent slip direction  $\langle 1\bar{1}0 \rangle$ . Interestingly, such slip systems have been observed.<sup>25</sup>

The present work is based on a few assumptions: (a) the system prior to the loading is dislocation free; (b) the model element  $M$  is characterized by a  $\text{bcc} \rightarrow \text{fcc}$  energy increase of 0.16 eV/atom; (c) the top and bottom layers of the simulated system are treated as rigid, which prevents dislocations from sweeping through; and (d) the system size is limited. Under these conditions, interesting phenomena such as the formation of slipped pipes and a  $\text{bcc} \rightarrow \text{fcc}$  transformation assisting further plastic deformation were observed. While further studies are needed to understand the effects of boundary conditions, loading algorithms, and pre-existing defect sources, it is particularly interesting to explore how the phase transformation deformation mechanism changes if one varies the energy difference between the bcc and fcc phases of the model element.

The observed yielding behavior of these films can be interpreted as a result of a competition for the strain energy to be released either as dislocation nucleation (plastic behavior) or free surface creation (interfacial fracture). For our system, the strain energy in  $M$  leads to the formation of dislocations and a phase change from bcc to fcc to promote further dislocation nucleation prior to activating the mechanism of film delamination. This behavior is greatly affected by numerous factors, including but not limited to the inter-

facial energy, the number and shape of defects at the interface, the initial crystallographic orientation, and the relative stiffnesses of the two layers.

In comparing a thin film that has larger stiffness relative to the substrate with one that is of lower stiffness, a stiffer material requires greater stress to strain; therefore, a higher strain energy is available for yielding/phase transformation behavior to occur. At the same time, the strain at the interface within the stiffer material would be lower than that for a more compliant material, which could make the interface more resistant to fracture. For thin films that are more compliant than their underlying substrates, less strain energy resides within the film, and it may not be sufficient to activate this slip mechanism.

#### IV. CONCLUSIONS

MD simulations have been carried out to study the delamination of a stiff bcc film from a Si substrate under tensile loading. The system was found to undergo elastic deformation, followed by an extensive yielding behavior before finally fracturing at the interface. The yielding is accompanied by dislocation emission from the interface to the inside of the film, whereas no dislocations were observed inside Si. As expected in bcc systems,  $\frac{1}{12}\langle 11\bar{1} \rangle \{\bar{1}21\}$  types of leading partial dislocations are seen to sweep through the crystal at the early stage of the loading, leaving behind slipped planes extending all the way to the interface. At later stages of the loading, however, the bcc film is seen to transform to a fcc lattice, and the leading partial dislocations become the  $\frac{1}{6}\langle 11\bar{2} \rangle \{111\}$  (reference to fcc lattice) types commonly seen in fcc systems. These dislocations in the bcc lattice have apparent slip planes of  $\{110\}$  and an apparent slip direction  $\langle 1\bar{1}0 \rangle$ . This observed yielding behavior is the result of the high strain energies achieved in the bcc material prior to fracture. Later, during crack propagation, the exposed Si exhibits wavy features indicative of a compliant behavior as the fractured regions attempt to relax to the unconstrained positions but are constrained by the unfractured regions that remain adhered to the film.

#### ACKNOWLEDGMENTS

This work was partially supported by the National Science Foundation Grant No. NSF\_CMMI 0800896. One of us (W.W.G.) would like to acknowledge the support of the Air Force through program Grant No. AOARD-08-4131 dedicated to understanding plasticity and fracture in hard materials and the Abu Dhabi–Minnesota Institute for Research Excellence (ADMIRE), a partnership between the Petroleum Institute (PI) of Abu Dhabi and the Department of Chemical Engineering and Materials Science of the University of Minnesota. Sandia is a multiprogram laboratory operated by Sandia Corporation, a Lockheed Martin Co., for the U.S. Department of Energy's National Nuclear Security Administration under Contract No. DEAC04-94AL85000.

<sup>1</sup>B. Cotterell and Z. Chen, *Int. J. Fract.* **104**, 169 (2000).

<sup>2</sup>A. Latapie and D. Farkas, *Modell. Simul. Mater. Sci. Eng.* **11**, 745 (2003).

<sup>3</sup>Yu. Ivanisenko, I. MacLaren, X. Sauvage, R. Z. Valiev, and H.-J. Fecht,

- Acta Mater.* **54**, 1659 (2006).
- <sup>4</sup>J. Tersoff, *Phys. Rev. B* **39**, 5566 (1989).
- <sup>5</sup>J. Tersoff, *Phys. Rev. B* **38**, 9902 (1988).
- <sup>6</sup>X. W. Zhou, H. N. G. Wadley, R. A. Johnson, D. J. Larson, N. Tabat, A. Cerezo, A. K. Petford-Long, G. D. W. Smith, P. H. Clifton, R. L. Martens, and T. F. Kelly, *Acta Mater.* **49**, 4005 (2001).
- <sup>7</sup>X. W. Zhou, R. A. Johnson, and H. N. G. Wadley, *Phys. Rev. B* **69**, 144113 (2004).
- <sup>8</sup>H. N. G. Wadley, X. W. Zhou, and W. H. Butler, in *Reactive Sputter Deposition*, edited by D. Depla and S. Mahieu (Springer-Verlag, Berlin, 2008), p. 497.
- <sup>9</sup>H. Balamane, T. Halicioglu, and W. A. Tiller, *Phys. Rev. B* **46**, 2250 (1992).
- <sup>10</sup>R. J. Jaccodine, *J. Electrochem. Soc.* **110**, 524 (1963).
- <sup>11</sup>J. D. H. Donnay and H. M. Ondik, *Crystal Data, Determinative Tables*, 3rd ed., Vol. 2, (U.S. Department of Commerce, National Bureau of Standards, and Joint Committee on Power Diffraction Standards, Swarthmore, PA, 1973).
- <sup>12</sup>I. Barin, *Thermochemical Data of Pure Substances* (VCH, Weinheim, 1993).
- <sup>13</sup>G. Simmons and H. Wang, *Single Crystal Elastic Constants and Calculated Aggregate Properties: A Handbook* (MIT, Cambridge, MA, 1971).
- <sup>14</sup>F. H. Featherston and J. R. Neighbours, *Phys. Rev.* **130**, 1324 (1963).
- <sup>15</sup>J. H. van der Merwe, *Prog. Surf. Sci.* **67**, 365 (2001).
- <sup>16</sup>L. Shen and Z. Chen, *Modell. Simul. Mater. Sci. Eng.* **12**, S347 (2004).
- <sup>17</sup>W. G. Hoover, *Phys. Rev. A* **31**, 1695 (1985).
- <sup>18</sup>K. Gall, M. F. Horstemeyer, M. Van Schliggaarde, and M. I. Baskes, *J. Mech. Phys. Solids* **48**, 2183 (2000).
- <sup>19</sup>J. Zimmerman, E. Webb, III, J. Hoyt, R. Jones, P. Klein, and D. Bammann, *Modell. Simul. Mater. Sci. Eng.* **12**, S319 (2004).
- <sup>20</sup>LAMMPS Molecular Dynamics Simulator, <http://lammps.sandia.gov/>
- <sup>21</sup>J. A. Zimmerman, C. L. Kelchner, P. A. Klein, J. C. Hamilton, and S. M. Foiles, *Phys. Rev. Lett.* **87**, 165507 (2001).
- <sup>22</sup>J. P. Hirth and J. Lothe, *Theory of Dislocations*, 2nd ed. (Wiley, New York, 1982), p. 368.
- <sup>23</sup>P. D. Bristowe and A. G. Crocker, *Philos. Mag.* **31**, 503 (1975).
- <sup>24</sup>D. Hull and D. J. Bacon, *Introduction to Dislocations*, 3rd ed. (Pergamon, Oxford, 1984), p. 121.
- <sup>25</sup>I. Kovács and L. Zsoldos, *Dislocations and Plastic Deformation*, 1st ed. (Pergamon, Oxford, 1973), p. 185.